Ultrahigh Efficiency Multiband Solar Cells

Final report for Director's Innovation Initiative project DII-2005-1221

March 29, 2006

Prepared by

J. W. Ager, Staff Scientist

W. Walukiewicz, Senior Staff Scientist

Kin Man Yu, Staff Scientist

Electronics Materials Program
Materials Sciences Division
Lawrence Berkeley National Laboratory

This work was supported by the Director's Innovation Initiative Program, National Reconnaissance Office, through the U.S. Department of Energy under Contract No. DE-AC02-05CH11231

Materials Sciences Division

ACKNOWLEDGEMENTS

LBNL staff on the project included Dr. Z. Liliental-Weber, Dr. W. Shan, Dr. O. Dubón, J. Beeman, I. D. Sharp, R. Farshchi, S. Li, and R. Jones. High quality ZnTe and ZnMnTe substrates were provided by Dr. P. Becla of MIT.

1 EXECUTIVE SUMMARY

The unique properties of the semiconductor ZnTeO were explored and developed to make multiband solar cells. Like a multijunction cell, multiband solar cells use different energy gaps to convert the majority of the solar spectrum to electrical current while minimizing losses due to heating. Unlike a multijunction cell, this is accomplished within a single material in a multiband cell. $ZnTe_{1-x}O_x$ films with x up to 2% were synthesized and shown to have the requisite unique band structure (2 conduction bands) for multiband function. Prototype solar cells based on an n-type $ZnTe_{1-x}O_x$ multiband top layer and a p-type ZnTe substrate were fabricated. Contacts to the cell and the series resistance of the substrate were identified as challenges for good electrical performance. Both photovoltage and small photocurrents were demonstrated under AMO illumination. A second semiconductor system, $GaN_xAs_{1-y-x}P_y$, was shown to have multiband function. This alloy system may have the greatest potential to realize the promise of high efficiency multiband solar cells because of the relatively advanced technology base that exists for the manufacturing of III-V-alloy-based IC and opto-electronic devices (including multijunction solar cells).

2 PROJECT BACKGROUND

The intrinsic power conversion efficiency limit for unconcentrated sunlight for a solar cell based on a single semiconducting material with a single junction is 31% [1]. In a conventional single junction solar cell one of the most important factors limiting power conversion efficiency is the loss of the sub-bandgap photons which are not absorbed by the material (and hence do not contribute to the cell power output). Great improvements have been achieved in reducing this loss by implementing the tandem (multijunction) cell concept in which semiconductors with different band gaps are stacked together, forming a series of solar cells (Fig. 1). Efficiencies approaching 40% are achieved with Ge/GaAs/GaInP triple junction (3J) cells under maximum concentration [2,3] and cells of this design are used in high-efficiency solar panels used on spacecrafts [4]. Development of 4-junction cells is progressing with the goal of achieving higher efficiencies. However, adding more junctions greatly complicates the cell designs and to date has led to only incremental improvements in efficiency [5].

To push solar cell efficiency to 40% and beyond, it is likely that new, so-called "3rd Generation" approaches will be required [6]. It has been proposed that the solar power conversion can be increased significantly by the introduction of additional states in the semiconductor band gap [7,8]. Such states provide a stepping-stone for sub-bandgap, low-energy photons to excite carriers across the gap via a two-step process. A simplified band diagram of a material with an intermediate band is shown in Fig. 1 with the three

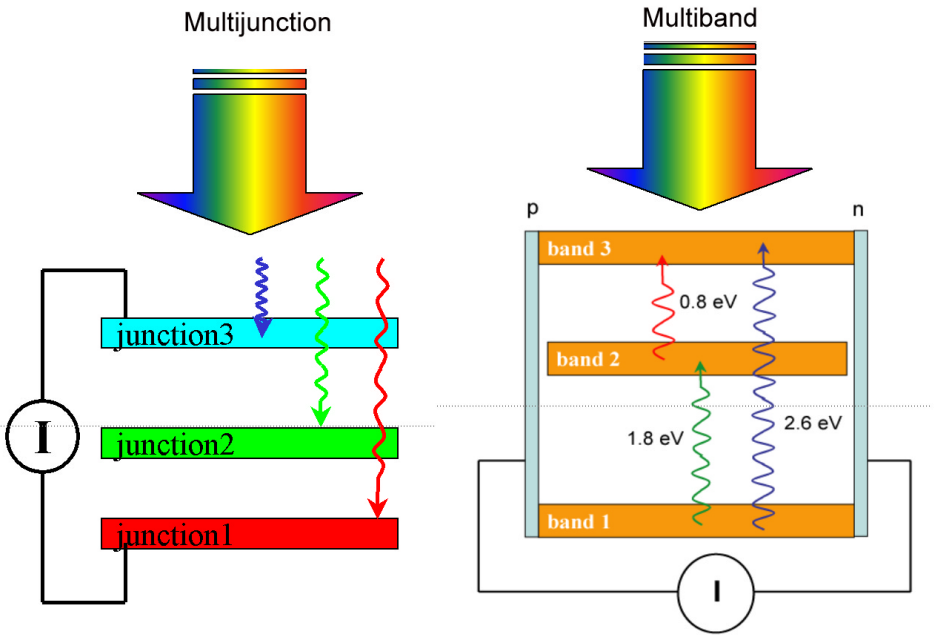

Fig. 1. Comparison of multijunction (MJ) and multiband (MB) semiconductor-based solar cells. In an MJ cell, there is a material with a single band gap at each junction. In a multiband cell there is one material with an intermediate band (band 2 in this depiction). In addition to the usual absorption from the valence to conduction band (1→3), solar radiation can also be absorbed (and converted to electrical energy) by the 2-photon process, 1→2 and 2→3, with the intermediate band 2 functioning as a "stepping stone." In this sense, a multiband solar cell is the functional equivalent of a 3J tandem cell but with a much simpler design and higher ultimate efficiency (Table 1).

Table 1. Theoretical maximum efficiencies for multijunction and multiband solar cells.

Design	Maximum thermodynamic efficiency[1,2,3,4]	Best laboratory demonstration[5,6]
Multijunction		
1 junction	41%	25%, Si and GaAs
2 junction	55%	30%
3 junction	62%	32% (37% at 175x)
Multiband		
3 bands	63%	
4 bands	72%	

[1]6000 K blackbody, 46,000x concentration
[2]C. H. Henry, "Limiting efficiencies of ideal single and multiple gap terrestrial solar cells," *J. Appl. Phys.* **51**, 4494 (1980)
[3]A. Luque and A. Marti, "Increasing the efficiency of ideal solar cells by photon induced transitions at intermediate levels," *Phys. Rev. Lett.* **78**, 5014 (1997).
[4]A. S. Brown *et al.*, "Limiting efficiency for a multiband solar cell containing three or four bands," *Physica E* **14**, 121 (2002).
[5]Standard AM1.5 conditions, 1x concentration, unless noted
[6]M. A. Green *et al.*, "Solar cell efficiency tables (version 25)," *Prog. Photovol. Res. Appl.* **13**, 49 (2005).

possible absorption steps indicated. As shown in Table 1, detailed theoretical calculations (performed for 46,000x concentration) indicate that with the proper location of the narrow intermediate band a single junction cell can achieve an ideal power conversion efficiency of 63.2%, much larger than the 55% ultimate limit for two junction tandem cells [7]. Even higher efficiencies of up to 71.7% have been predicted for materials with two bands of intermediate states [8].

Until very recently, practical realization of semiconductors with this multi-band structure had not been achieved [9]. However, work by LBNL has shown that a new class of semiconductor materials – highly mismatched alloys (HMAs) [10,11,12] – are ideally suited for making multiband semiconductors. HMAs are formed by the isoelectronic substitution of a small fraction (typically less than 10%) of one element in a compound semiconductor by another whose electronegativity is very different: the best-studied example is the replacement of up to 5% of As by highly electronegative N to form the GaN_xAs_{1-x} alloy. In these materials, the electronic band structure of the alloys is drastically modified by small changes in the alloy composition.

A multiband semiconductor needs to have two conduction bands which are separated in energy (bands 2 and 3 in Fig. 1). Figure 2 illustrates how this is accomplished by the incorporation of O into the II-VI semiconductor ZnTe. Oxygen does not "fit" into the electronic structure of ZnTe due to its small size and large electronegativity. Instead, when it is incorporated at low concentrations, it forms a

localized level located within the ZnTe band gap. At higher oxygen concentrations, the level becomes a narrow band of extended states, which is exactly the new band required for multiband function [13]. The oxygen level interacts with the conduction band, "pushing" it up in energy while at the same time it is pushed down in energy. In addition to the O content, Mn alloying can also be used to adjust the energy level positions, as shown in Fig. 3. Thus, band locations corresponding to those that are optimal for a multiband solar cell can be produced in ZnTeO and ZnMnTeO. In this FY05 Director's Innovation Initiative (DII) project, we thoroughly investigated the ZnTeO multiband system and identified the technological development path for using this material in multiband solar cells.

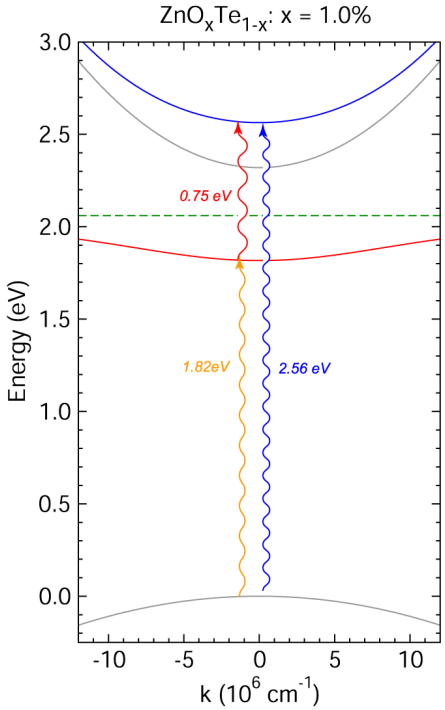

Fig. 2. Band anticrossing and formation of an intermediate band in ZnO_xTe_{1-x}. When oxygen is incorporated at low concentrations, it forms a localized level (green dashed line) within the band gap of ZnTe. At higher concentrations the level interacts with the ZnTe conduction band (gray line). The "band anticrossing" interaction produces two new bands. The lower band is derived from the oxygen level (red line). The upper band (blue solid line) is derived from the original conduction band and is pushed up in energy by the interaction with the lower band. The presence of the intermediate band and the energy shift of the upper band are monitored by the optical transitions from the valence band at 1.8 eV (E_-) and 2.6 eV (E_+). The third transition (at 0.7 eV) is also shown (red line).

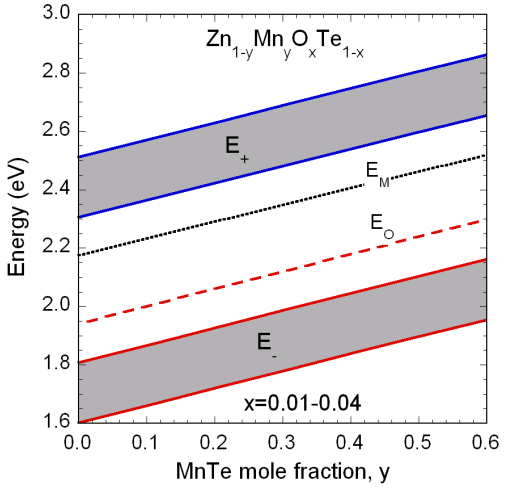

Fig. 3. Illustration of band gap tuning in the multiband semiconductor $Zn_{1-y}Mn_yTe_{1-x}O_x$. The energy positions of the ZnMnTe band gap and the position of the isolated oxygen level are shown as a function of Mn content y as dotted and dashed lines, respectively. The variation of the E_- and E_+ transitions for oxygen contents between 1 and 4 % are indicated by the grey regions. At a given value of y, increasing x decreases the E_- transition energy and increases the E_+ transition energy.

3 PROJECT TECHNICAL PLAN

The project had 4 technical tasks which are summarized as follows.

1. **Develop $ZnO_{1-x}Te_x$ and $Zn_yMn_{1-y}O_xTe_{1-x}$ as multiband semiconducting alloys.** We have discovered that ion implantation followed by pulsed laser melting (PLM) is an efficient way to synthesize the highly non-equilibrium stoichiometries required for multiband semiconductors and employed this process in the work reported here.
2. **Fabricate solar cells using this material.** Bulk p-type ZnTe and ZnMnTe substrates were used as a p-type side of the solar cell junction. The n-type ZnOTe layer was fabricated by co-implanting O with group VII donors (Cl) followed by pulsed laser melting (PLM) of the implanted layer. The thickness and the doping levels of the n-type layer were optimized for the maximum solar cell performance.
3. **Test AM0 power efficiency and compare to theoretical models of the behavior of this novel solar cell design.** Prototype solar cell junctions were fabricated and tested.
4. **Develop other multi-band semiconductors based on the concept of highly mismatched alloys.** Consideration of possible III-V HMAs suitable for multiband solar cells led to the identification of $GaAs_{1-x-y}N_xP_y$ with y in the range of 0.3-0.5. This material was synthesized by the implantation+PLM technique and shown to be a multiband semiconductor.

4 PROJECT ACCOMPLISHMENTS

4.1 Multiband $Zn_yMn_{1-y}O_xTe_{1-x}$

Our method for creating the non-equilibrium conditions required to synthesize $Zn_{1-y}Mn_yO_xTe_{1-x}$ alloys is ion implantation followed by single-pulse laser melting (PLM). The technique is illustrated schematically in Fig. 4. Significant effort was invested in optimizing the implantation as well as the PLM conditions to produce a uniform and n-type $Zn_{1-y}Mn_yO_xTe_{1-x}$ top layer on a p-type $Zn_{1-y}Mn_yTe$ substrate for use in device testing. We have significant technical understanding of the PLM process from our prior work on III-V and II-VI semiconductors. If the laser fluence is too low, there will be incomplete melting of the implanted layer and the regrowth will initiate from implant damaged material and the regrown layer will be highly defective. If the fluence is too high, we observe an increasing roughening of the surface, which can be caused by the formation of oxygen bubbles or the partial ablation of the implanted material. Also, high fluence may also prolong the melt duration causing the O to out-diffuse, leading to reduced incorporation in the regrown layer. In the III-V and II-VI systems we have studied to date, a fluence in the range of 0.2 – 0.5 and 0.08-0.3 J cm^{-2}, respectively has been found to yield alloyed material of high structural quality.

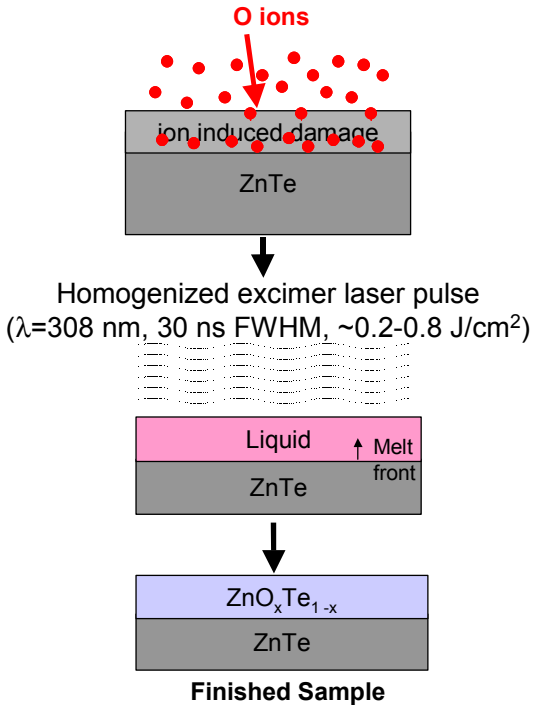

Fig. 4. Schematic illustrating formation of a ZnOTe layer by ion implantation of O ions followed by single pulse laser melting (PLM). The liquid surface layer regrows epitaxially from the underlying crystal on time scales on the order of 10^{-7} seconds. Such time scales mitigate secondary phase formation, even when the concentration of the implanted species greatly exceeds its equilibrium solubility limit. Thus, thin films with highly non-equilibrium stoichiometries can be made by this method.

Our typical characterization protocol is to use photomodulated reflectance (PR) to determine the multiband nature of the $Zn_{1-y}Mn_yO_xTe_{1-x}$ layer and to evaluate layer quality. The effect of varying the laser fluence on the PR spectrum is shown in Fig. 5. At laser fluences below 0.04 J/cm^2, no melting occurs and the no PR signal is observed from the heavily implant-damaged top layer. At laser fluences above 0.08 J/cm^2, melting occurs, some O substitutes on the Te site, and $Zn_{1-y}Mn_yO_xTe_{1-x}$ with an intermediate band is formed. The two observed transitions, E_- and E_+, are from the $Zn_{1-y}Mn_yO_xTe_{1-x}$ valence band to the intermediate band and to the conduction band, respectively (see Fig. 2). The observation of these two peaks is definitive evidence of the formation of an

intermediate band and, hence, of a multiband semiconductor. The PR peaks become narrower at still higher fluences, which is indicative of higher layer quality; the small shift to lower energy of E_+ indicates possibly a small loss of substitutional O. Finally at the laser fluences >0.5 J/cm^2 ablation occurs; the E_- and E_+ transitions diminish while the E_M transition from the substrate $Zn_{1-y}Mn_yTe$ appears.

In order to confirm the calculated implantation profiles and to evaluate Cl (n-type dopant, see below) and O redistribution following laser melting, secondary mass ion spectrometry (SIMS) measurements were performed on the O and Cl co-implanted ZnTe samples after PLM. The SIMS data are shown in Fig. 6. Prior to PLM) both measured profiles are in good agreement with the implantation simulation, except near the surface, where SIMS analysis is known to be inaccurate. After PLM, the regrowth front can be observed as a step at a depth of 150 nm below the surface. This is in perfect

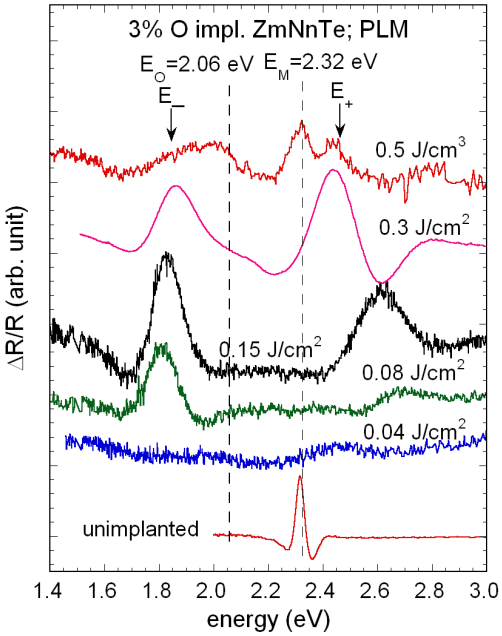

Fig. 5 Effect of laser fluence on photoreflectance spectrum of $Zn_yMn_{1-y}O_xTe_{1-x}$ with $y = 0.12$. The bandgap E_M of unimplanted material ($x = 0$) is 2.32 eV. PLM incorporates O on the Te site, splitting the conduction band into E_- and E_+, which are observed as peaks at 1.8 and 2.5 eV. The most uniform PR spectrum is obtained at a laser fluence of 0.3 J cm^{-2} in these experiments.

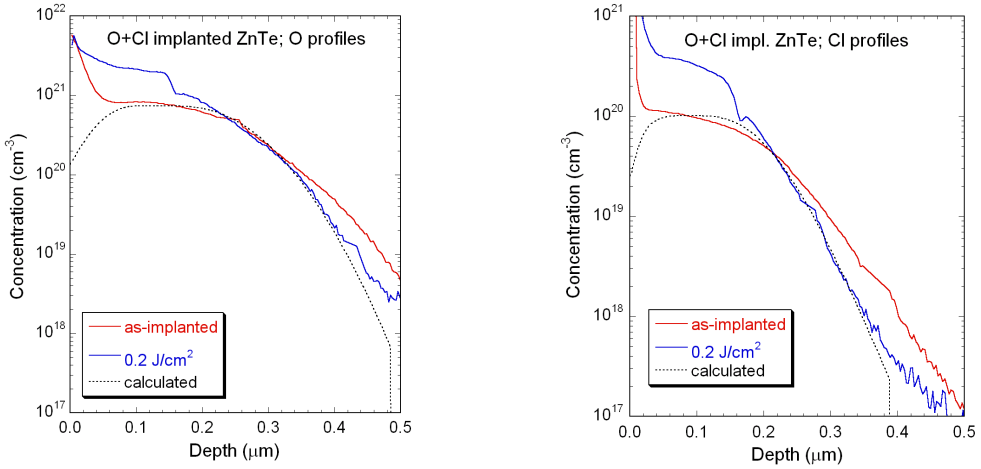

Fig. 6. Secondary Ion Mass Spectroscopy (SIMS) analysis of ZnTe implanted with O and Cl. Prior to laser melting, both measured profiles (O, left; Cl, right) are in good agreement with the implantation simulation, except near the surface, where SIMS analysis is known to be inaccurate. After annealing, the regrowth front can be observed as a step at a depth of 150 nm below the surface. The oxygen content appears to have increased after laser annealing. Because the annealing is done in air, the effect may be due to incorporation of oxygen from the ambient. The apparent increase in the Cl concentration is not understood at this time. Both the O and Cl profiles are relatively flat (factor of 2) in the laser regrown area and the step at the regrowth front is relatively abrupt.

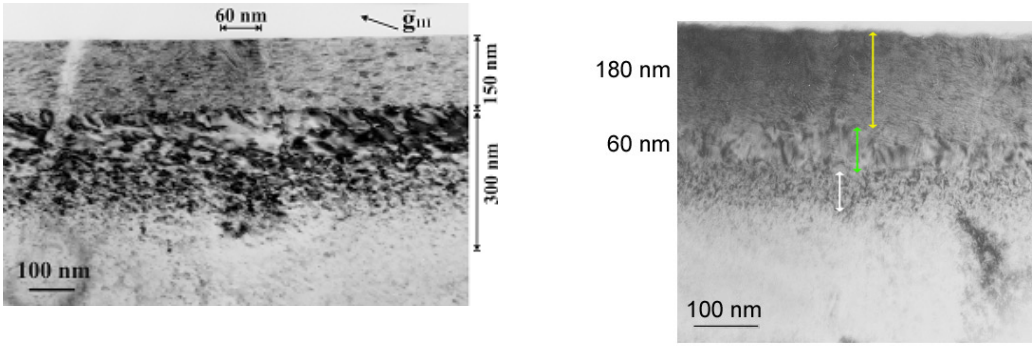

Fig. 7. (a) Transmission electron microscopy of cross-sectional samples for a Cl+O implanted ZnTe sample after PLM with energy fluence =0.2 J/cm^2. The melt front is seen to initiate at 150 nm below the surface under these conditions. Implantation damage is seen ca. 200 nm below this point. (b) Cross-section TEM micrograph showing regrowth in ZnOTe after laser melting (at 0.3 J/cm^2). Optimized implantation and annealing conditions were employed. High quality regrowth initiates 240 nm below the surface and extends for 60 nm (green arrow). The remaining 180 nm are regrown but with some defects, as evidenced by the mosaic or mottled pattern.

agreement with the transmission electron microscope (TEM) image obtained for the same sample (Fig 7(a)). The oxygen content appears to have increased after PLM. Because the annealing is done in air, this effect may be due to incorporation of oxygen from the ambient. This observation opens up an interesting opportunity for the PLM synthesis of $Zn_{1-y}Mn_yO_xTe_{1-x}$: it may be possible to form this alloy by PLM of $Zn_{1-y}Mn_yTe$ alone in a controlled oxygen environment without the O^+-implantation process. The apparent increase in the Cl concentration is not understood at this time. It is also possible that the SIMS yields were different in the PLM layer. Both the O and Cl profiles are relatively flat (factor of 2) in the laser regrown area and the step at the regrowth front is relatively abrupt. This latter feature is desired for optimal diode behavior.

We performed further characterization with transmission electron microscopy (TEM) and found that our initial implantation and PLM conditions were not optimal. Our initial oxygen implant was performed under conditions such that the damage extended to approximately 0.35 μm below the surface. However, the TEM (Fig. 7(a)) and SIMS (Fig. 6) analyses showed that the epitaxial regrowth front began only 150 nm below the ZnTe surface (i.e. at the depth where the crystal was damaged). In order to form a high quality ZnO_xTe_{1-x} layer it is desirable to melt through the damage layer so that epitaxial regrowth can be initiated from an undamaged region of the crystal. To achieve this, we designed a "shallower" implantation protocol and combined it

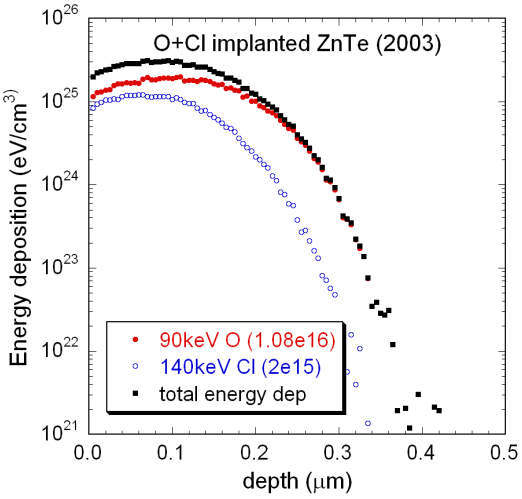

Fig. 8 Calculated energy deposition of optimized Cl+O implantation conditions. The damage depth (deposited energy >1x10^{24}eV/cm^3) extends < 0.3 μm below the surface.

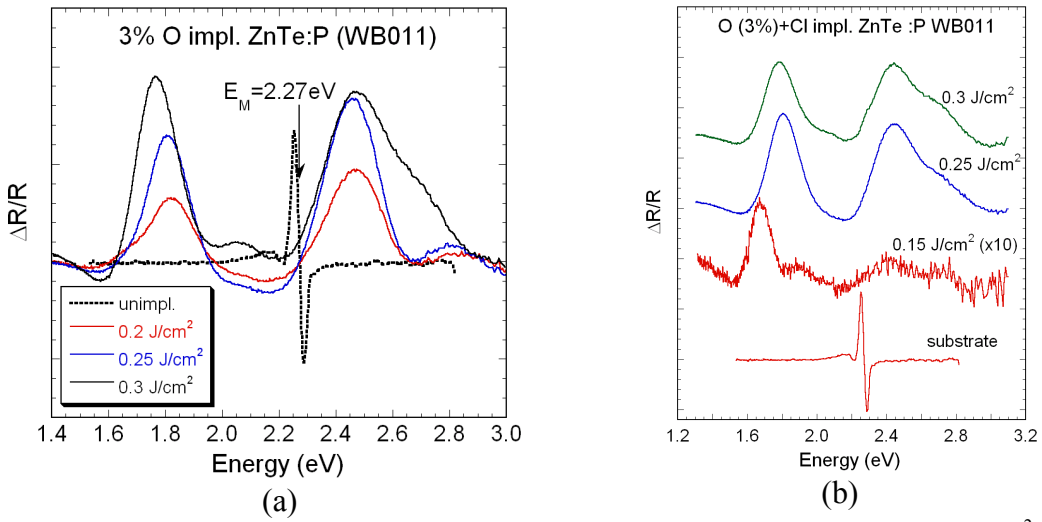

Fig. 9 (a) PR spectra from O implanted ZnTe after PLM with fluences of 0.2, 0.25 and 0.3 J/cm^2. E_- and E_+ bands at ~1.8 and 2.5 eV from the ZnOTe layer are observed. The splitting between these peaks is proportional to the O incorporation, which is the highest at the highest laser fluence used. (b) PR spectra from O and Cl co-implanted ZnTe samples after PLM with laser fluences of 0.15, 0.25 and 0.3 J/cm^2. Addition of Cl, which is required to form a n-type top layer, does not affect the multiband nature of the epilayer.

with a higher laser energy fluence (0.275 J/cm^2) for use with p-type ZnTe substrates. The calculated O and Cl implantation profiles (O is required to form the multiband structure; Cl is required to make the surface layer n-type)for this more optimal protocol, which was designed to limit implant damage to within 300 nm of the surface, are shown in Fig. 8.

We tested the new implantation procedure in two steps: (1) O implantation only and (2) O and Cl implantation. Photoreflectance (PR) data shown in Fig. 9(a) after the O implantation step reveal the expected $E_-$and E_+ bands at ~1.8 and 2.5 eV from the ZnOTe layer formed with the optimized implantation conditions. Having confirmed that the new implantation conditions lead to the formation of a good quality ZnOTe layer, we performed Cl and O co-implantation into p-type ZnTe and ZnMnTe substrates. The co-implanted samples were then processed by PLM with laser energy fluences in the range of 0.15-0.35 J/cm^2. PR from a series of O and Cl co-implanted ZnTe samples after PLM are shown in Fig. 9(b). We observed that the PR signals from the sample after PLM with 0.15 J/cm^2 are weak. This is expected because with this relatively low fluence the regrowth depth is smaller than the damaged layer and thus the quality of the regrown layer is poor. A ZnOTe layer with good quality is obtained by PLM with fluence of ~0.25 J/cm^2 as shown by the strong PR signals and the relatively sharp transitions. From the energy position of the intermediate band (E_- transition), we estimate the oxygen content in these layers to be ~2%. The PR spectra of ZnOTe and ZnOTe:Cl are very similar (both have the two transitions indicative of a multiband semiconductor), indicating Cl doping does not degrade the optical properties

The structural quality of the ZnOTe:Cl layer was characterized by TEM, as shown in Fig. 7(b). The depth at which the regrowth front initiated was found to be 240 nm below the surface; however some end of range defects from the implant were found up to 300 nm from the surface. As a result, the regrowth was not completely optimal. The first 60 nm regrew with high structural quality, but defects were found in the next 180 nm

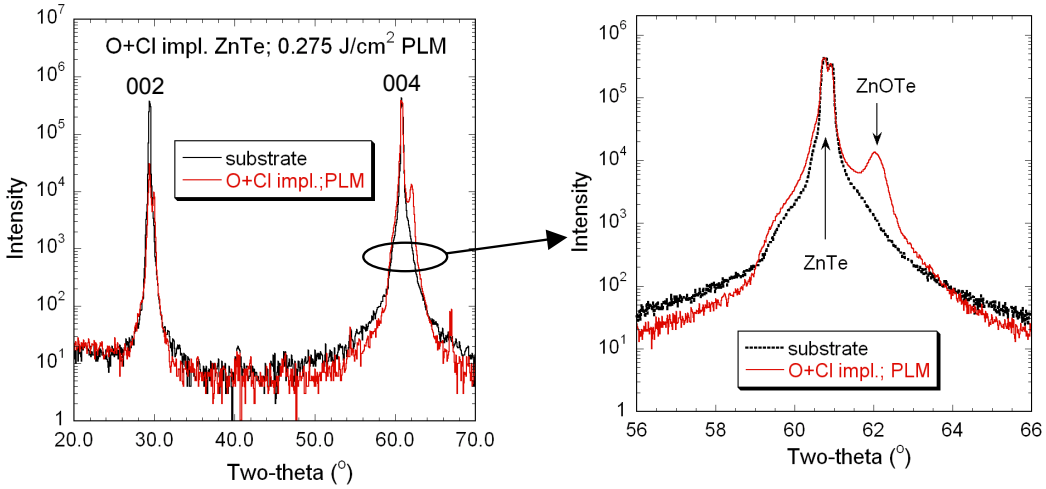

Fig. 10. X-ray diffraction of ZnOTe. The appearance of a peak from the ZnOTe layer at higher angle (smaller lattice spacing) confirms the existence of substitutional O on the Te site in the lattice. There are with no observable precipitates (ZnO, ZnCl, ZnTe, etc.) or polycrystal grains.

towards the surface. We conclude that the laser melts most, but not all, of the O and Cl implanted regions. This is a marked improvement over our previous implantation and PLM protocol; under these conditions the epitaxial regrowth front began at a heavily damaged region located 150 nm below the ZnTe surface. As shown in Fig. 10, X-ray diffraction (XRD) on a (001)-oriented ZnTe bulk crystal with a ZnOTe:Cl epilayer shows only extra diffraction peaks at higher diffraction angle compared to the (002) and (004) diffraction peaks of the substrate ZnTe. This confirms the formation of ZnO_xTe_{1-x} layer with a smaller lattice parameter with no polycrystalline secondary phases.

In summary, we have achieved good quality ZnOTe:Cl thin films on p-type ZnTe

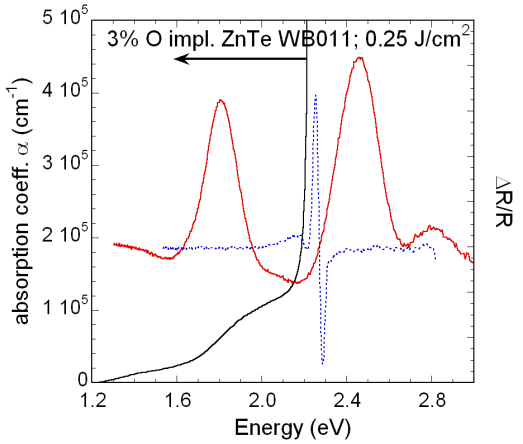

Fig. 11 Absorption (left axis) spectra from a O implanted ZnTe sample. The dotted line is the PR from the ZnTe substrate (right axis). The two transitions from the samples after PLM at ~1.8 and 2.5 eV arise from the E_- and E_+ bands in the ZnOTe layer.

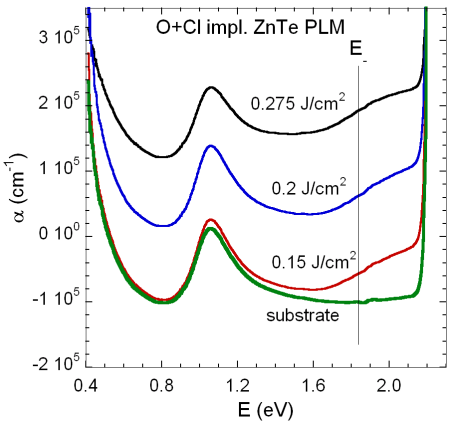

Fig. 12. Absorption spectra of ZnTeO made by ion implantation/pulsed laser melting. The sharp peak at ~1 eV is a transition from a spin-orbit split band to the top of the valence band in the p-type substrate. Vertical line indicates position of E^-. E_+ could not be observed due to absorption by the substrate. Spectra are offset for clarity

substrates. We discuss now more detailed optical characterization of our "best" films. We further investigated the optical characteristics of the ZnOTe by optical absorption. Figure 11 shows the optical absorption spectrum of one such ZnOTe layer. The PR spectrum from the same sample is also shown. Optical absorption from the lower subband of the ZnOTe layer is readily observed at 1.7 eV. It is significant that the absorption coefficient of this band is relatively large ($\alpha \sim 10^5$ cm^{-1}); this value is similar to that obtained above the bandgap in direct gap materials and shows that the subband has sufficient absorption to function as the intermediate level in a multiband solar cell. Notice also that the absorption from the upper subband is not observable here due to the strong absorption of substrate ZnTe at 2.27 eV. We expect both of the conduction bands of ZnTeO to have considerable direct gap character. Figure 12 shows a series of absorption spectra from O+Cl implanted ZnTe substrates followed by pulsed laser melting. The absorption at the E_- transition (valence band to lower conduction band) is strong: >5x10^4 cm^{-1}, corresponding to an absorption depth of approximately 0.5 μm. Higher absorption at E_- is observed for samples processed at higher laser fluences; this is due to the thicker ZnOTe layers that are formed. The absorption feature at ~1 eV corresponds to a transition from the spin-orbit split band to the top of the valence band in the p-type ZnTe substrate.

It is noteworthy that we have not been able to observe photoluminescence (PL) from the n-type ZnTeO:Cl layers that we have made in the course of the project by PLM. It should also be mentioned that only very weak (or not observable) PL signals are observed from our ZnTe (ZnMnTe) substrate materials. Therefore, it is important to study as to whether it is possible to observe photoluminescence (PL) from II-VI alloy layers made by ion implantation and pulsed laser melting (PLM). To investigate whether this is true, in general, for layers made by PLM, we investigated CdSeO. CdSe is known to have strong PL, even in the presence of surfaces, such as in CdSe quantum dots. CdSe single crystals were implanted with 3% O and processed by PLM by our collaborators at Harvard University (Aziz group). A schematic band diagram for CdOSe alloy is shown in Fig. 13. The O localized level is located above the conduction band edge; we would expect the incorporation of O to reduce the band gap. As shown in Fig. 14, optical transitions from both the valence band and the spin-orbit split valence band to the O induced E_- band are clearly observed. We estimate the O incorporation to be in the 1-2% range.

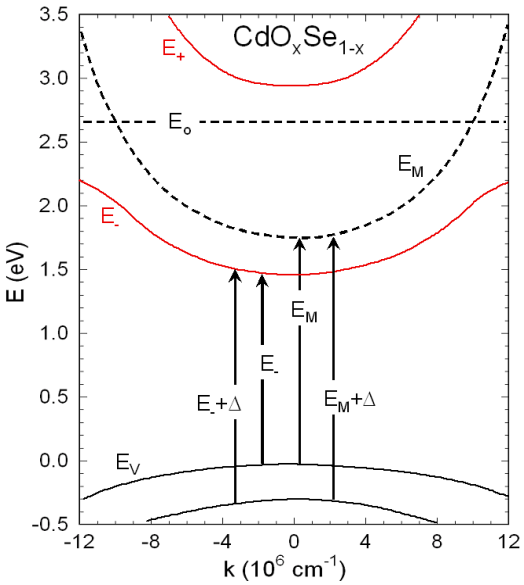

Fig. 13 A schematic energy band diagram for CdO_xSe_{1-x} formed by O implantation and PLM. The expected optical transitions are also illustrated. The O content is expected to be 1-2%.

Photoluminescence (PL) from the same series of samples are shown in Fig. 15. For energy fluences >1.2 J/cm^2 band edge PL from CdSeO is clearly observed, demonstrating that PL can be obtained from thin films of highly mismatched semiconductors synthesized by the PLM process.

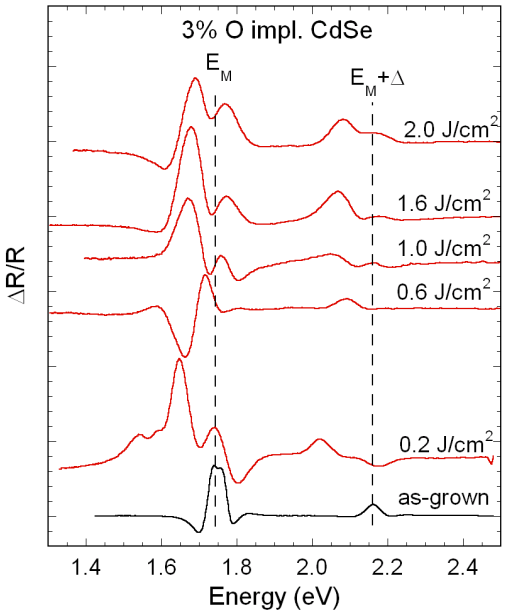

Fig. 14. Photoreflectance (PR) from a series of CdSe samples as-grown and implanted with 3% O followed by pulsed laser melting with laser fluence in the range of 0.2 to 2.0 J /cm^2. Dotted lines indicate the transitions from the valence band to the conduction band (1.75 eV) and from the spin-orbit split valence band (2.15 eV) in CdSe without O.

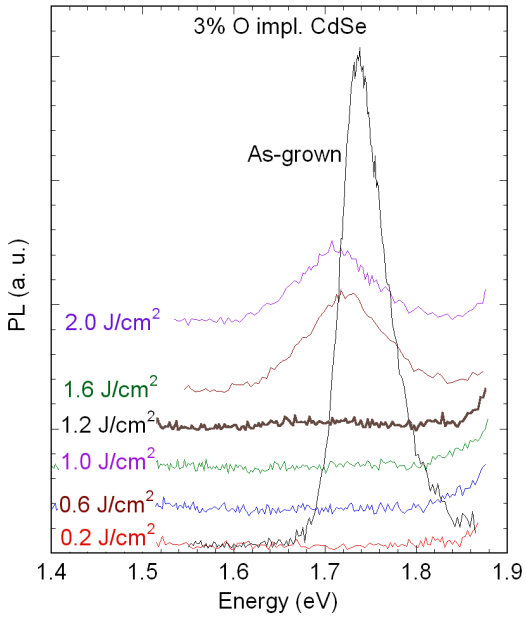

Fig. 15 Photoluminescence (PL) from the same series of samples as in Fig. 14. Band edge PL is clearly observed in CdSeO for laser fluences of 1.6 and 2.0 J cm^{-2}.

4.2 Fabricate multiband solar cells

Test structures for solar cell testing were fabricated; one of our test structures is shown in Fig. 16. Electrical testing under dark conditions was used to confirm the presence of a n-p junction between the n-type ZnOTe:Cl layer and the p-type substrate. One of the key issues we found through our I-V studies is the necessity of forming a good ohmic contact to the n-type ZnOTe:Cl layer. We investigated two approaches: (1) a transparent oxide contact layer and (2) a metal contact in either a grid-structure or as a point contact.

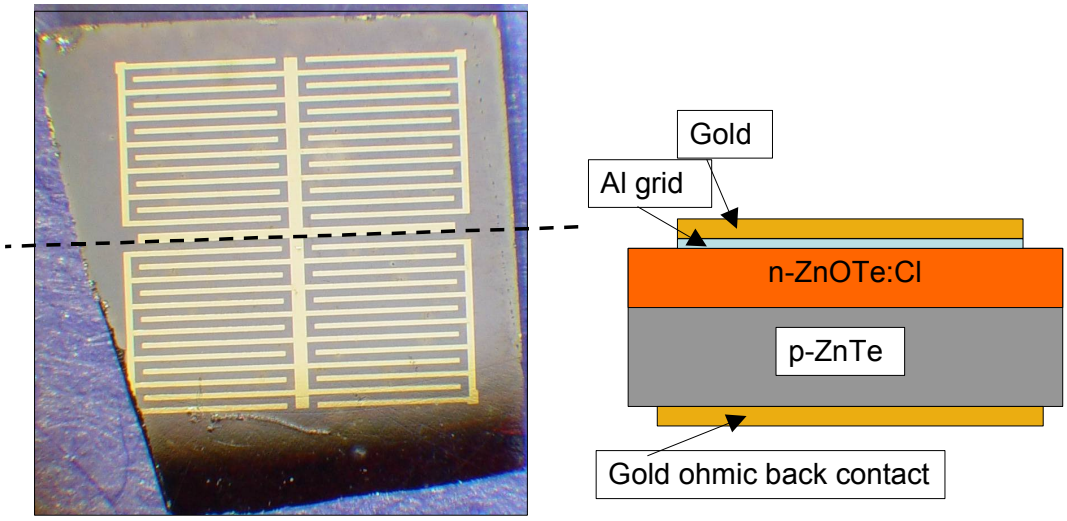

Fig. 16. Left: a top-view photograph of a test cell: p-ZnTe substrate with 200 nm thick n-ZnTeO top layer. The grid structure is Al/Au and forms an ohmic contact on the ZnOTe. . Right: a cross-sectional schematic of the photograph on the left.

We examined n-ZnO and indium tin oxide (ITO) and as potential transparent, conducting top contacts. ZnO and ZnO doped with Al were investigated. An important issue is the thermal budget of the ZnTeO structure. Our initial work has shown the optical quality of the device is stable to annealing temperatures of at least 350°C Sputtered Zn metal layers were oxidized by thermal annealing in an oxygen ambient at a series of temperatures up to 400°C to form ZnO. These ZnO films have the proper energy gap but were found to be too resistive to use as top contacts to a ZnOTe solar cell. However, we succeeded in making a transparent top contact for a p-ZnTe/n-ZnTeO:Cl solar cell structure using sputtered indium tin oxide (ITO) with an electron concentration in the 10^{20} cm^{-3} range. Dark I-V curves were similar to those obtained with metal top contacts. However, a linear section of the semilog IV plot indicting ideal diode behavior under forward bias was not observed with ITO top contacts.

Overall, devices with metal contacts performed better than those made with the transparent top contact approach described above. We measured dark I-V curves using a number of metals including Al and In and with both point and grid contact geometries. Our best I-V curves were measured for structures we have grown on relatively low resistivity p-ZnTe substrates (ρ=1 Ω-cm) that we obtained from Germany; these devices had a with contact resistance of approximately 1 kΩ. Figure 17 shows our "best" I-V

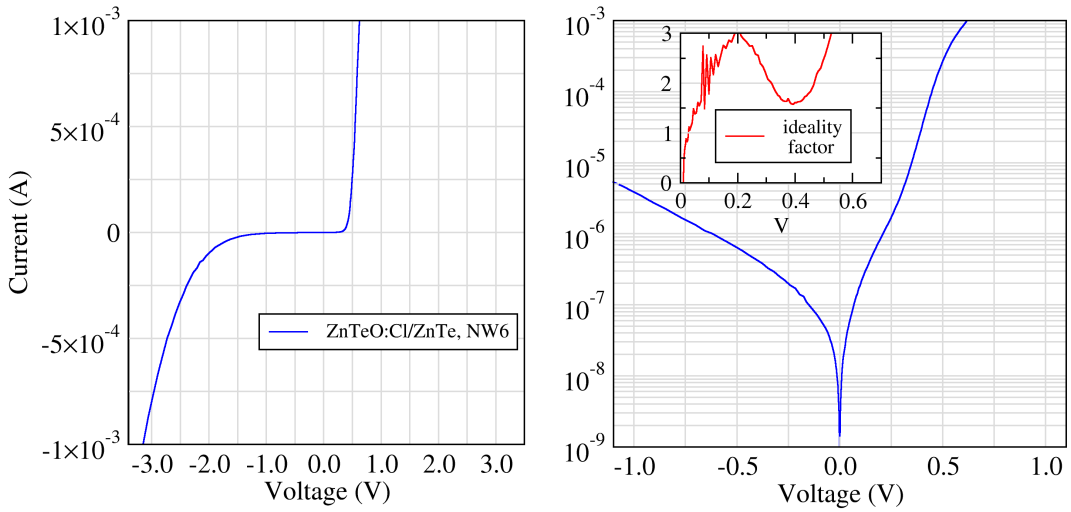

Fig. 17. Current-voltage measurements performed on a ZnTeO:Cl/p-ZnTe diode structure with optimized contacts. The diode ideality factor under forward bias is shown in the inset.

curves obtained to date. The ideality in this linear regime is close to 2 (inset of Fig. 17), indicating that it is determined by carrier recombination. This data implies that although contacts and series resistance are a processing challenge, it is possible to make a "good" diode with the n-ZnTeO/p-ZnTe heterojunction.

However, the series resistance of the substrate and the quality of the regrown layer emerged as challenges in achieving photocurrent under illumination. Figure 18 compares current voltage (IV) measurements for two ZnTeO/ZnTe devices and a Si solar cell. It is clear that the lower resistivity substrate reduces resistance under forward bias (1 kΩ vs. 2.5 kΩ). However, the resistance is still approximately 10x higher than in the Si solar cell. Our data shows that the substrate has a high resisitivity, which reduces the forward current in the diode and also will compromise charge collection in a solar cell. We initiated growth on lower resistivity ZnTe epilayers grown on GaAs to address this issue.

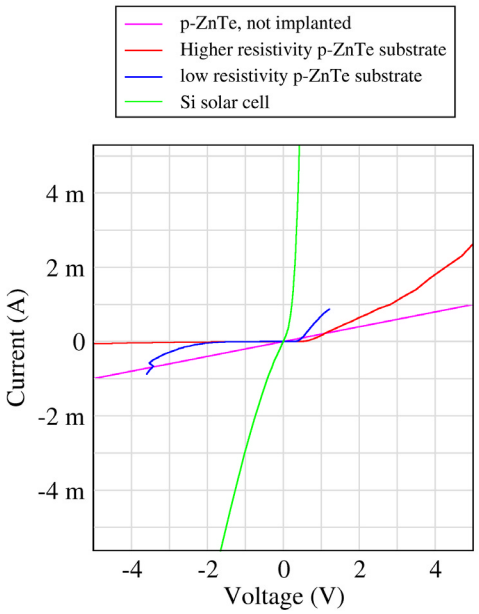

Fig. 18. Dark IV curves for ZnTeO:Cl (n-type) layers grown by pulsed laser melting on p-type ZnTe substrates. Data for the p-ZnTe substrate is shown, indicating its ohmic behavior. A smaller current in forward bias is observed for layer grown on a higher resistivity substrate. Data from a commercial Si solar cell is shown for comparison. The series resistance is much lower.

4.3 Test AM0 power efficiency

Photovoltage (Fig. 19) and photocurrent (Fig. 20) measurements were performed on Cl-doped ZnO_xTe_{1-x}/p-ZnTe diode structures. An optimized contact geometry was employed and the substrate was thinned by mechanical polishing before measurement. A photoreflectance spectrum from this diode is also shown in Fig. 19. The E_- and E_+

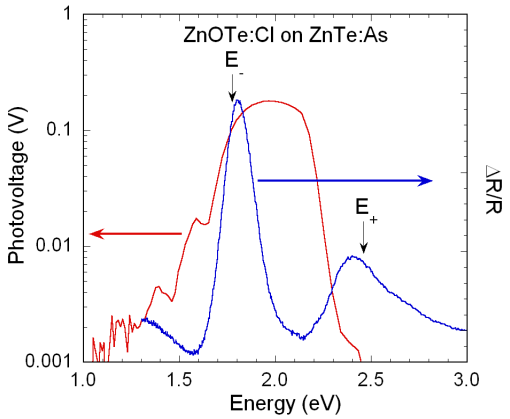

Fig. 19. Photovoltage (red trace, left axis) and photoreflectance (blue trace, right axis) measurements performed on a ZnTeO:Cl/p-ZnTe diode structure with optimized contacts. Clear photovoltaic response is observed in the vicinity of the E- transition (valence band to intermediate band) of the ZnTeO:Cl layer.

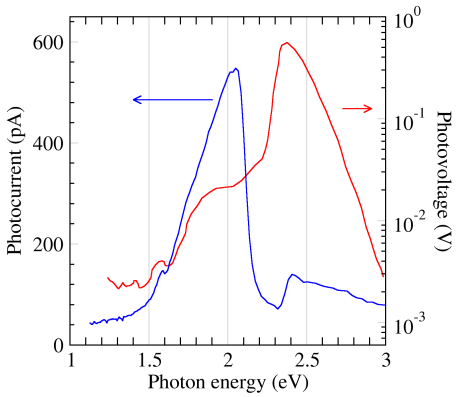

Fig. 20. Photocurrent (blue trace, left axis) and photovoltage (red trace, right axis) generation at E_- from ZnMnTeO made by PLM at a fluence of 0.3 J/cm^2. The spectral response of the photocurrent is observed at both E_- (1.5-2.0 eV) and at E_+ (2.4 eV). We attribute the weaker PC signal in the E_+ region to a stronger surface recombination effect due to shorter penetration depth of incident light.

transitions of the multiband ZnOTe top layer are located at ca. 1.75 and 2.45 eV, respectively. Comparison of the photovoltage and PR spectra in Fig. 19 establishes that there is a clear photovoltaic response in the vicinity of the E_- transition (valence band to intermediate band). This shows that there is a direct transition from the valence band to the intermediate band. The photocurrent measurement shown in Fig. 20 demonstrates that electrons in the intermediate band are sufficiently mobile to produce a current. Both these observations are consistent with the band structure presented in Fig. 2. We note that the decrease of the PV response for photon energies >2 eV is due to the limited instrument response in that energy range.

Figure 21 shows the AM0-illuminated IV curve for a n-ZnTeO/p-

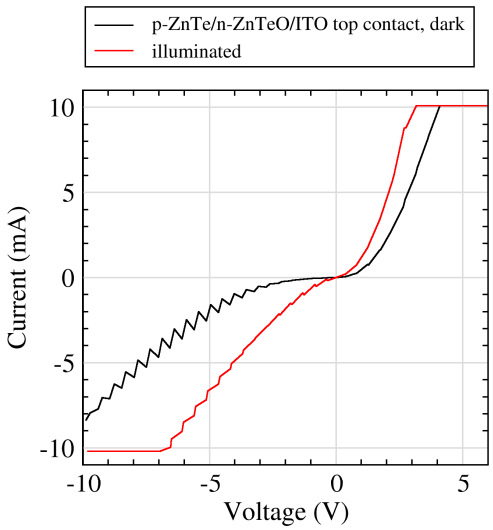

Fig. 21. Dark and illuminated IV curves for a n-ZnTeO/p-ZnTe multiband device with an ITO top contact. Charge separation is not observed.

ZnTe device fabricated with an ITO contact. A current at zero applied voltage (I_{SC}) from charge separation at the pn junction is not observed. Similar results were found for devices with metal contacts. We believe that series resistances from the contacts and the substrate are primarily responsible for the failure to observe charge separation in these devices. The devices that will be fabricated on low resistivity ZnTe epilayers are expected to have better performance in this regard.

4.4 Develop other multi-band semiconductors

Since III-V materials have a well developed technology base, a III-V multiband material system would be very attractive for the development of high efficiency solar cells. We considered carefully whether a multiband solar cell could be made from a III-V semiconductor alloy. For high efficiency multiband solar cells the intermediate band (band 2 in Fig. 1) must be narrow; a narrow band can be formed only from states that are located well below the conduction band edge. N substitution into GaAs has been used to form the HMA $GaAs_{1-x}N_x$. This material has been investigated thoroughly [12] and has been used to make commercial vertical cavity light emitting lasers (VCSELS) [14]. However, in this case the localized states are located in the conduction band, resulting in a relatively wide lower subband and making this alloy unsuitable for a multiband solar cell.

We performed a comprehensive analysis of the opportunities for making a multiband III-V material and identified N substitution into $GaAs_{1-y}P_y$. as a candidate system. Figure 22 shows the calculated energy levels of the N level (E_N) and the Γ, X, and L conduction bands of $GaAs_{1-y}P_y$ alloy as a function of P content y. At a P content of > 0.3, the energy level that will be produced by small amounts of nitrogen, E_N, lies below the main conduction band E^Γ of the $GaAs_{1-y}P_y$ alloy; this is precisely the condition that is required to make the narrow intermediate band desirable for a multiband solar cell. An upper limit to the P content is set by the appearance of an indirect band gap ($E^X < E^\Gamma$) at y > 0.5. The most promising $GaAs_{1-y}P_y$ alloy composition for making high efficiency multiband solar cells is thus shown in shaded area in Fig. 22 ($0.3 < y < 0.5$).

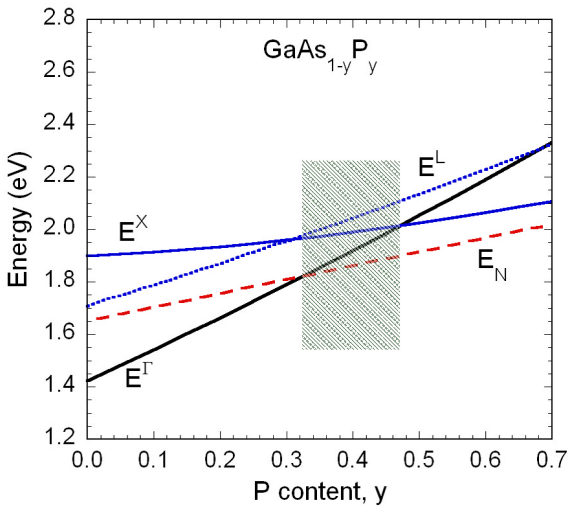

Fig. 22 Calculated energy positions of the N level and the Γ, X, and L conduction bands of the $GaAs_{1-y}P_y$ alloy system. At a P content y of > 0.3 the local N level E^N drops below the conduction band E^Γ, creating the conditions required to make a multiband semiconductor. An upper limit to the P content is set by the appearance of an indirect band gap ($E^X < E^\Gamma$) at y > 0.5.

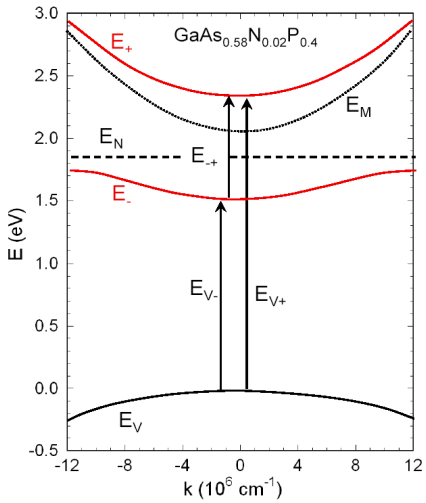

Fig. 23 A schematic diagram of a $GaAs_{0.58}P_{0.4}N_{0.02}$ highly mismatched alloy (HMA) illustrating the splitting of the original conduction band E_M into E_+ and E_- due to the interaction of the N level E_N with E_M. The 3 optical transitions that can be used for power generation – E_{V-}, E_{V+}, and E_{-+} – are also shown.

In the last quarter of the DII project, we investigated the potential of the $GaN_xAs_{1-y-x}P_y$ alloy system to make multiband solar cells. . A schematic band diagram for a $GaAs_{1-y}P_y$ multiband semiconductor y = 40% and an N content of 2% ($GaAs_{0.58}N_{0.02}P_{0.4}$) is presented in Fig. 23. The energy positions of the bands are calculated by the band anticrossing (BAC) model [10,11]. The three possible optical absorptions in this case are 0.8 eV ($E_-\rightarrow E_+$), 1.5 eV ($E_V\rightarrow E_-$) and 2.3 eV ($E_V\rightarrow E_+$). A theoretical maximum efficiency of between 55% and 60% can be achieved for this alloy by controlling the amount of N substituted on the anion (As or P) site.

Figure 24 shows a series of PR spectra from $GaAs_{1-y}P_y$ samples with $0\le y\le 0.38$ implanted with 2% of N followed by PLM and rapid thermal annealing [15]. The energy gap, E_M of as-grown $GaAs_{1-y}P_y$ and the N level E_N are indicated in the figure. Similar to the case of O^+-implanted ZnTe we reported earlier, PR spectra from the N^+-implanted $GaAs_{1-y}P_y$ samples (y>0) also show two well resolved optical transitions E_- and E_+, distinctly different from the band gap transition of the substrate materials. The locations of E_+ and E_- vary as the P content increases. It is also important to note the change in the relative strength of these two transitions. In GaAs and in As-rich $GaAs_{1-y}P_y$ the E_- transition is much stronger than E_+ transition. However as is seen in Fig. 24 the relative strength of the E_+ transitions increases with increasing P content and becomes stronger than E_- for y>0.25. This behavior can be easily explained by the band anticrossing (BAC) model, taking into account the

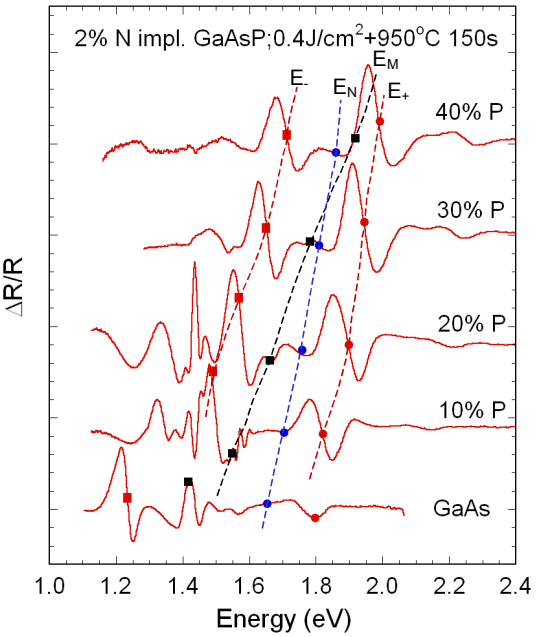

Fig. 24 Photoreflectance spectra from 2% N implanted $GaAs_{1-y}P_y$ (y=0 to 0.4) PLM at 0.4 J/cm^2 followed by 950°C 150s RTA. Positions of the E_- and E_+ transitions as well as the various energy levels (substrate bandgap E_M and N level E_N) are also indicated in the figure. In each spectrum, E_M indicates the position of the conduction band relative to the valence band in unimplanted material. A conduction band splitting of 0.3 and 0.4 eV is achieved in $GaAs_{0.7}P_{0.3}$ and $GaAs_{0.6}P_{0.4}$, respectively

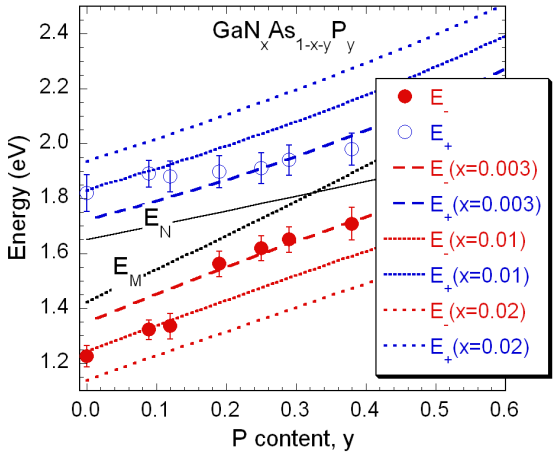

Fig. 25 Measured values of the E_- and E_+ transitions in GaNAsP are shown as closed and open circles, respectively. The solid curves show the positions of the conduction band minimum at the Γ point E_M for the $GaAs_{1-y}P_y$ substrate and the N level E_N . Calculated values of the E_- and E_+ transitions based on the BAC model for x=0.003, 0.01 and 0.02 are also shown.

much weaker dipole optical coupling of the valence band to E_N compared with the coupling between the valence band and E_M.

The energy values of the E_- and E_+ transitions for the $GaN_xAs_{1-x-y}P_y$ layers (Fig. 24) are shown in Fig. 25 as closed and open circles, respectively. The solid curves show the positions of the conduction band minimum at the Γ point E_M for the $GaAs_{1-y}P_y$ substrate and the N level E_N. Calculated values of the E_- and E_+ transitions based on the BAC model for x=0.003, 0.01 and 0.02 are also shown. It can be seen that E_+ follow E_N at low and E_M at larger P contents. On the other hand E_+ transitions mostly follow E_N at low and E_M at lager y. The character of the wavefunctions and thus also the strength of the optical transitions depend on the location of the E_- and E_+ states relative to E_N and E_M.

Comparison between the calculated and measured E_+ and E_- values in Fig. 25 shows that for $GaAs_{1-y}P_y$ layers with y≤0.12 ~1% of N is incorporated in the film (~50% of the total implanted N). For $GaAs_{1-y}P_y$ layers with y>0.12, the incorporated N concentration is smaller (x=0.003), and corresponds to an activation efficiency of 15% of the implanted N. Although only small fraction of N (x=0.003) is incorporated in $GaAs_{1-y}P_y$ layers with y > 0.2 using the present implantation-PLM conditions, strong and distinctive optical transitions are indeed observed, confirming the predicted multiband function for these compositions.

It should be noted that in order to make an intermediate band solar cell with this alloy the N content x in $GaN_xAs_{1-x-y}P_y$ has to be >0.01 so that the transition between the E_+ and E_- band covers the energy range >0.65 eV. In the final months of the project, we focused on synthesizing $GaN_xAs_{1-x-y}P_y$ alloys with higher N concentration. Two approaches were taken:

(i) increasing the total implanted N
(ii) varying the PLM energy fluence.

Figure 26 shows that by doubling the total implanted N from 2% to 4% in GaAs the E_- transition decreases by ~70 meV. This corresponds to an increase in total active N, x from 0.01 to 0.018. However, a much smaller effect on the increase in x (from 0.0039 to 0.0049) is observed for $GaAs_{0.62}P_{0.28}$ with the corresponding increase in the total implanted N from 2% to 4%.

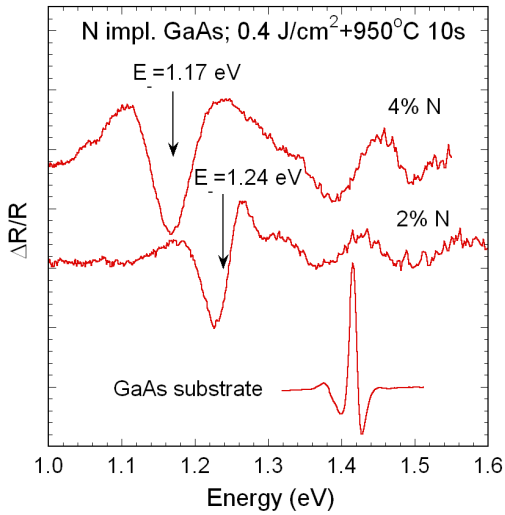

Fig. 26 PR spectra from 2 and 4% N implanted GaAs samples after PLM at 0.4J /cm^2 followed by 950°C for 10s. The band gap shifts by 70 meV when the implanted N increases from 2% to 4% .

We have shown previously that reducing the energy fluence for the PLM process results in an increase in the amount of incorporated N in GaAs, provided that the energy fluence is above the melting threshold of GaAs. This effect is illustrated in Fig. 27, in which the active N concentration (x) in 4% N implanted GaAs is graphed as a function of PLM energy fluence. We believe the effect is associated with the duration of the melt during the PLM pulse, which is longer at higher fluences. The longer melt duration that occurs at higher energy fluences enables the N atoms to migrate to the surface or to coalesce and form bubbles (i.e., N-related voids) and thus reduces N activation in N implanted GaAs.

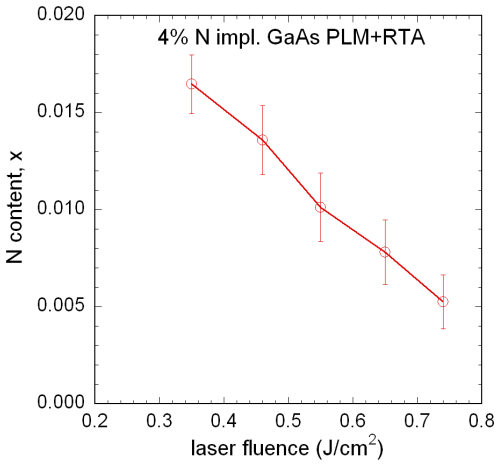

Fig. 27 Active N concentration (x) determined from PR measurements in 4% N implanted GaAs as a function of PLM energy fluence. The samples were annealed at 950ºC for 10 sec. following the PLM process.

However, in N implanted GaAsP alloys a similar effect of energy fluence on the N incorporation was not observed. Only small changes in the energy positions of E_- and E_+ are observed in 4% N implanted $GaAs_{0.62}P_{0.38}$ samples as the energy fluence varies from 0.3 to 0.5 J/cm^2. That is, the increase in the N activation with decreasing laser fluence observed in GaAs is not observed in the GaAsP alloys. We suspect that this effect may be due to the high density of the misfit dislocations in the $GaAs_{1-y}P_y$ epitaxial layers, which form during film growth due to the large lattice mismatch with the GaAs substrate (>0.4% for y>0.12). It is possible that these dislocations may act as a sink for the preferential segregation of N during the PLM and RTA processing steps. This may be the cause of the low activation efficiency of implanted N in $GaAs_{1-y}P_y$ samples with y>0.15. To alleviate the effect of dislocations in the epitaxial layers, our colleagues at the University of San Diego are growing $GaN_xAs_{1-x-y}P_y$ alloys on GaP substrates (GaP has a smaller lattice mismatch than GaAs) using gas-source MBE technique. In addition, the n-type doping of $GaN_xAs_{1-x-y}P_y$ alloys is being investigated by co-implanting S with N in GaAsP films.

5 TECHNOLOGICAL OUTLOOK

An optimized multiband semiconductor-based solar cell has a higher ultimate efficiency than either the currently produced 3-junction (3J) or developmental 4J cells and thus presents a significantly new approach to achieving ultrahigh efficiency for space power conversion applications. At this point, the potential of an optimized cell for high efficiency operation is unknown. However, the higher ultimate efficiency coupled with the simple single junction structure of this design compared to any practical tandem MJ concept has the promise of a very high intelligence payoff in terms of compact and high efficiency solar cells for space and other applications.

Multiband function and photocurrent and photovoltage at 2 of the 3 transitions in ZnTeO-based multiband cells were demonstrated. Contacts to the cell and the series resistance of the substrate were identified as challenges for good electrical performance. When these are overcome, the crucial issues of the optimal electron population of the intermediate band and the carrier lifetime in that band can be investigated in detail. Compared to any other multiband approach, the ZnTeO is the most developed to date and can form the basis of this critical feasibility tests.

Ultimately, we believe that the GaNAsP alloy system may have the greatest potential to realize the promise of high efficiency multiband solar cells based on the following factors.

- III-V materials are used as the basis for numerous optoelectronic applications including high efficiency multijunction solar cells, lasers, light emitting diodes, etc. Compared to other compound semiconductors, the thin film deposition technologies – metal organic chemical vapor phase deposition (MOCVD) and molecular beam epitaxy (MBE) – are mature and reliable. Moreover, it has been demonstrated that alloys with compositions close to that we are targeting here –GaNP [16], GaNAs [17], and GaInNP [18] – can be made by MBE. For these reasons, we believe that optimal cell designs can be rapidly transferred to a production environment.
- As discussed in this report, optimization of a multiband solar cell will require careful consideration of doping levels, layer thicknesses, contacts, and other device-level considerations. In assessing these, one can build on decades of experience in III-V device design and production-scale manufacturing. For example, we are confident that n and p doping levels can be achieved using standard dopants used in similar III-V-based devices.

As an example of the technology path that is achievable using III-V based highly mismatched alloys, we consider the development of near-IR lasers that utilize the InGaAsN alloy system. Incorporation of N into GaAs and InGaAs was first achieved in the mid-1990's and unusual effects on the band structure were noted. However, the technical development path was accelerated by the 1999 LBNL work that established the mechanism (band anticrossing) by which N incorporation reduces direct band gap into the near-IR region of interest for optical communication [10]. The quantitative predictions of the band anticrossing (BAC) model were then used by Infineon to develop a commercial vertical cavity emitting laser (VCSEL) only a few year later [14]. We expect a development path that could be at least this rapid for the application of III-V

based multiband semiconductors in high-efficiency solar cells once a operating high efficiency prototype is demonstrated.

An important consideration is the efficiency that could be obtained in a fully developed III-V-based multiband solar cell compared to current (and near-future) multijunction solar cells. As shown in Table 1, a multiband cell (3-band) has a similar ultimate efficiency as a 3 junction tandem cell. It is rather early in the technological development path to predict what percentage of a multiband cell ultimate efficiency can be achieved in practice; this contrasts with the high state of development of multijunction cells achieved after over 15 years of development. However, there are two important considerations that suggest that a higher practical efficiency can be achieved in a multiband cell as compared to a multijunction cell. (1) A design for a prototype III-V-based multiband cell is shown in Fig. 28. This design has only 4 semiconductor layers plus metal contact. This contrasts with much more complex structure of a multijunction cell (up to 20 layers). In the case of a multiband cell, the simplicity of the design will allows material growers to concentrate on improving the quality of a much smaller number of layers. This, in turn, may lead, as the technology matures, to the realization of a higher percentage of a greater proportion of the design's ultimate efficiency. (2) For space applications, both beginning of life (BOL) and end of life (EOL) efficiencies are important. The latter efficiency is determined primarily by the radiation resistance of the cell design [19]. At this point the radiation resistance of a multiband cell is untested. However, a multiband design is expected to involve a smaller volume of active material compared to a multijunction design. It is possible that multiband cells may be more radiation resistant than multijunction cells for this reason, although further study will be required.

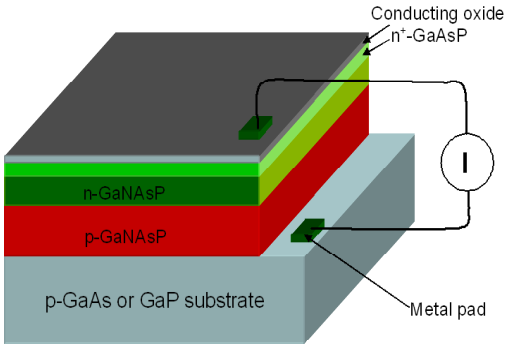

Fig. 28. Prototype multiband solar cell based on GaNAsP. All active layers in the cell can be grown by molecular beam epitaxy.

5 REFERENCES

1 Shockley, W. and H. A. Queisser, *J. Appl. Phys*. **32**, 510 (1960).

2 Kurtz, S. R., D. Myers, J. M Olson, *Proc. 26th IEEE Photovoltaic Specialists Conf.*, (IEEE, New York, 1997) p 875-8.

3 Green, M. A., K. Emery, K. L. King, S. Igari, and W. Warta, "Solar Cell Efficiency Tables (Version 21)," *Prog. Photovolt: Res. Appl.* **11**, 39-45 (2003).

4 Marvin, D. C., "Assessment of Multijunction Solar Cell Performance in Radiation Environments," Aerospace Report No. TOR-2000(1210)-1.

5 King, R.R., P. C. Colter, D. E. Joslin, K. M. Edmondson, D. D. Krut, N. H. Karam, and Sarah Kurtz, *Proc. 29th IEEE Photovoltaic Specialists Conf.*, New Orleans, 2002 (IEEE, New York, 2002) pp. 852-5.

6 Green, M. A., *Prog. Photovolt.* **9**, 123-135 (2001).

7 Luque, A. and A. Marti., "Increasing the Efficiency of Ideal Solar Cells by Photon Induced Transitions at Intermediate Levels," *Phys. Rev. Lett.*, **78**, 5014 (1997).

8 Brown, A. S., M. A. Green and R. P. Corkish, "Limiting efficiency of a multi-band solar cell containing three or four bands," *Physica* E **14**, 121, (2002).

9 Cuadra, L., A. Marti, and A. Luque, "Present status of intermediate band solar cell research," *Thin Solid Films* **451-452**, 593 (2004).

10 Shan, W., W. Walukiewicz, J. W. Ager III, E. E. Haller, J. F. Geisz, D. J. Friedman, J. M. Olson, and S. R. Kurtz, "Band anticrossing in GaInNAs alloys," *Phys. Rev. Lett.* **82**, 1221-1224 (1999).

11 Walukiewicz, W., W. Shan, K. M. Yu, J. W. Ager III, E. E. Haller, I. Miotlowski, M. J. Seong, H. Alawadhi, and A. K. Ramdas, "Interaction of localized electronic states with the conduction band: Band anticrossing in II-VI semiconductor ternaries," *Phys. Rev. Lett*. **85**, 1552 (2000).

12 Ager III, J. W., and W. Walukiewicz, "Current status of research and development of III-N-V semiconductor alloys," *Semicond. Sci. Technol*. **17**, 741-745 (2002) and references therein.

13 Yu, K. M., W. Walukiewicz, J. Wu, W. Shan, J. W. Beeman, M. A. Scarpulla, O. D. Dubon, and P. Becla, "Diluted II-VI Oxide Semiconductors with Multiple Band Gaps," *Phys. Rev. Lett.* **91**, 246403 (2003)

14 Riechert, H., A. Ramakrishnan, and G. Steinle, "Development of InGaAsN-based 1.3 μm VCSELs," *Semicond. Sci. Technol.* **17** 892 (2002).

15 Yu, K. M., W. Walukiewicz, J.W. Ager III, D. Bour, R. Farshchi, O. D. Dubon, S. X. Li, I. Sharp, and E. E. Haller, "Multiband GaNAsP Quaternary Alloys," *Appl. Phys. Lett.* **88**, 092110 (2006).

16 Bi, W.G., and C.W. Tu, "N incorporation in GaP and band gap bowing of GaN_xP_{1-x}", *Appl. Phys. Lett.* **69**, 3710 (1996).

17 Bi, W.G., and C.W. Tu, "Bowing parameter of the band-gap energy of GaN_xAs_{1-x}", *Appl. Phys. Lett*. **70**, 1608 (1997).

18 Hong, Y.G, A. Nishikawa, and C. W. Tu, "Effect of nitrogen on the optical and transport properties of $Ga_{0.48}In_{0.52}N_yP_{1-y}$ grown on GaAs(001) substrates", *Appl. Phys. Lett*. **83**, 5446-5448 (2003).

19 See, for example, D. C. Marvin, "Assessment of Multijunction Solar Cell Performance in Radiation Environments," Aerospace Report TOR-2000(1210)-1.